Article:
Walther, T. and Krysa, A.B. (2017) Transmission electron microscopy of AlGaAs/GaAs quantum cascade laser structures. Journal of Microscopy , 268 (3). pp. 298-304. ISSN: 0022-2720

https://doi.org/10.1111/jmi.12655

Transmission electron microscopy of AlGaAs/GaAs quantum cascade laser structures

Thomas Walther[1,3] and Andrey B Krysa[2,3]

[1] Kroto Centre for High Resolution Imaging and Analysis,
[2] EPSRC National Centre for III/V-Technologies,
[3] Department of Electronic and Electrical Engineering, University of Sheffield, UK

Abstract

Quantum cascade lasers can be efficient infrared radiation sources and consist of several hundreds of very thin layers arranged in stacks that are repeated periodically. Both the thicknesses of the individual layers as well as the period lengths need to be monitored to high precision. Different transmission electron microscopy have been combined to analyse AlGaAs/GaAs quantum cascade laser structures in cross-section. We found a small parabolic variation of the growth rate during deposition, affecting the stack periodicity and a reduced aluminium content of the AlGaAs barriers, while their widths as well as those of the GaAs quantum wells agreed with the nominal values within one atomic layer. Growth on an offcut substrate led to facets and steps at the interfaces.

Lay summary

Quantum cascade lasers can be efficient infrared radiation sources and consist of several hundreds of very thin layers arranged in stacks that are repeated periodically. Both the thicknesses of the individual layers as well as the period lengths need to be monitored to high precision, and we use transmission electron microscopy at medium and atomic spatial resolution as a post-growth quality control tool.

Introduction

Quantum cascade lasers (QCLs) provide effective multiple quantum well emission sources for the infrared range based on inter-subband transitions of electrons rather than electron-hole recombination as used in other types of solid state lasers (Faist et al. 1994) and are presently considered for applications in terahertz imaging (Tonouchi 2007). Under an applied bias, electrons travelling through the structure can emit low-energy photons (hence, infrared radiation) each time they lose energy when traversing a thin barrier into the next quantum well. A sequence of electron injection and active emission layers consists of typically a dozen quantum wells and barriers within a period that itself is then repeatedly stacked, typically fifty times to several hundred times, so a single electron can generate many photons. This yields a structure consisting of several hundreds or even thousands of individual layers the epitaxial growth of which needs to be controlled to high precision (at the scale of fractions of monolayers, which physically would mean for the group III sub-lattice in AlGaAs atomic planes with mixed Ga/Al occupancies) during hours of growth. The essential problems to be investigated relate to

i) the ***avoidance of structural defects***, such as dislocations,
ii) the ***reproducibility of a given growth rate*** over extended time durations (in our case, for a growth run delivering a series of three wafer structures), maintaining the over-all thicknesses of the periodic stacks from the first to the last period,
iii) the growth of barrier layers with ***sub-atomic precision in thickness*** to enable electron tunnelling through them with a certain probability and
iv) the minimization of interdiffusion to maintain ***sharp interfaces***.

For all these points transmission electron microscopy (TEM) is necessary, as macroscopic techniques such as X-ray diffraction run into ambiguities in modelling when the parameters in the top and the bottom of the layer stacks differ. The main experimental challenge is that all high-resolution imaging techniques have a limited field of view and so cannot address all points simultaneously. For planar illumination TEM, the largest two-dimensional digital detectors presently have ~8000 pixels in a row, and if 0.28 nm lattice fringes are to be imaged at twice the Nyquist limit, i.e. at 4 pixels per fringe, then the total field of view will be limited to ~560 nm, which is almost an order of magnitude smaller than the QCL structure in this study. Analogue detectors such as negative plates can cover a slightly larger area with lattice resolution but suffer from geometrical distortions near the corners due to the objective / projector lens systems (Hue et al. 2005). Moreover, it is impossible to produce perfectly flat specimens, and thickness and focus changes over the field of view induced by wedge-shaped specimens can entail contrast changes and even contrast reversals in lattice images that are difficult to control and can make the interpretation of interfaces difficult. For focused illumination in scanning TEM (STEM) mode, the corresponding limit will be given by the number of image data points the scan generator can handle (maximum number of lines times maximum number of rows).
Hence, many electron microscopy studies of QCL structures are limited to overview images covering 300-600 nm field of view at relatively low resolution (Barvosa-Carter et al. 2001, Inoue et al. 2004), or medium-resolution imaging of a small number, n, of periods, e.g. $n = 1$ (Manz et al. 2005; Revin et al. 2011), $n = 2$ (Cao et al. 2008), $n = 3$ (Liu et al. 2000), $n = 4$ (Xu et al. 2008) and $n = 5$ (Matmon et al. 2010). Lattice imaging is usually restricted to regions < 40 nm in extent (Green et al. 2004; Kandaswamy et al. 2008; Terachima and Hirayama 2009). Cross-sectional scanning tunnelling microscopy (STM) has also been used to provide atomic resolution maps of cleaved surfaces (Barvosa-Carter et al. 2001) but is again restricted to small clean areas in cross-sections of sphalerite semiconductors that cleave well.
In summary, there is no single atomic scale imaging technique that can image an area several microns in length, so that images from different length scales need to be correlated to provide not only a pretty image but a true quality control tool for QCL growth.

Experimental

While QCLs have traditionally been grown by molecular beam epitaxy, it was shown by Green et al. (2004) that metal-organic vapour phase epitaxy can also be used to reproducibly grow the required ~1nm thin layers needed for QCLs.
We have studied an AlGaAs/GaAs QCL structure of 55 periods, each consisting of 8 GaAs quantum wells and 8 AlGaAs barriers (i.e. 880 fine layers in total) sandwiched

between two thicker 600 nm GaAs layers, all grown by metal-organic chemical vapour deposition at 690 ºC via an InGaP buffer on a GaAs(001) substrate with a nominal offcut of 10 º towards (111)A. The offcut was employed to suppress CuPt type ordering in the $In_{0.49}Ga_{0.51}P$ cladding layers which were used for the optical laser studies. Several samples were grown consecutively in the same chamber. As precursors we used trymethyl group-III compounds and phosphine and arsine for the group-V elements. More details of electrical contacts and optoelectronic measurements are provided in the letter by Krysa et al. (2011).
A cross-sectional sample for TEM was prepared by standard sandwiching, cutting, grinding, mechanical polishing and low-angle argon ion milling until foil perforation. We then used bright- and dark- field transmission electron microscopy (BF/DF-TEM) to address issue (i), high-resolution electron microscopy (HREM) to study (iii) & (iv) and annular dark-field scanning transmission electron microscopy (ADF-STEM) to study points (ii) & (iv). Electron microscopy was performed using two instruments: a JEOL 2010F field-emission (S)TEM at 197kV (with Gatan GIF200, Gatan 794 multi-scan charge coupled device (CCD) 1k × 1k camera and Gatan Digiscan I for scanning TEM) and a double aberration-corrected cold-field emission JEOL Z3100 R005 STEM at 300kV (with Gatan Tridiem ER GIF Model 865, Gatan Ultrascan 1000 2k × 2k CCD camera and Gatan Digiscan II for STEM operation).

Results

Investigations of several adjacent areas by BF and ADF STEM at the lowest possible magnification that does not suffer from de-scan problems and so yields homogeneous contrast over the field of view, have not shown any dislocations, hence the dislocation density must be $<< 10^7$ cm^{-2}. This is expected for an almost perfectly lattice matched system such as AlGaAs/GaAs. In ADF STEM, GaAs appears brighter than AlGaAs due to the higher average atomic number (*Z*-contrast), however, note the difference in the appearance of the two thick GaAs layers in Figure 1, indicating a wedge shaped geometry of the sample whose thickness decreases from the bottom towards the top near the free surface.

In BF and 002 DF TEM imaging of thin regions, the AlGaAs appears brighter than the GaAs; for the BF case this is due to its lower mass-density and in DF it is due to the increase of the 002 structure factor contrast with increasing Al content. This explains the similarity of aligned image sections of BF and(002 dark field images as in Figure 2, from which the MQW periods near the top of the stack have been measured as 45 ± 0.6 nm. Because of the aforementioned contrast reversals with increased specimen thickness it has not been possible to image layers at the centre or bottom of the stack in conventional TEM under similar (kinematical) conditions.

The two thinnest AlGaAs barriers above the thicker AlGaAs injection layers (all dark) are clearly visible in the nine stacks of the medium-magnification ADF-STEM image shown in Figure 3. For the acquisition the specimen had to be tilted ~ 2 º off the precise <100> zone axis to show the interfaces in thicker parts of the specimen edge-on. This is due to the wafer offcut, however, the nominal offcut would have meant an ~ 7 º tilt about would have been necessary. As *Z*-contrast is less prone to contrast reversals with thickness and focus changes than coherent phase imaging (Pennycook and Jesson 1991) it has been possible to compare period lengths in the whole stack, as tabulated in Table 1. From this it can be seen that the stacks are ~47nm wide in the

middle but only ~45nm near bottom and top of the structure. This indicates a ~ 2 % parabolic variation of the growth rate during deposition, the initial and final growth rates being ~ 1 % smaller than the average of 46nm/stack, while the growth rate in the middle was ~1% enlarged. In the line profile of Figure 3b we plot the square root of the ADF intensity from Figure 3a (after background subtraction so that the ADF detector recorded zero for regions without specimen, ensured by briefly closing the gun valve and so switching off the illumination, cf. Walther (2006), Qiu et al. (2011)) as function of the growth direction. The dotted parabolic line gives an approximate envelope of the intensity expected for pure GaAs with an average atomic number of $<Z_{GaAs}> = 32$, as fitted to the layers of maximal image contrast. For an $Al_xGa_{1-x}As$ alloy the average atomic number is given by $<Z_{AlGaAs}> = 32–9x$, so that, assuming perfect Rutherford scattering where the intensity scales with Z^2 and neglecting amorphous surface oxides which could reduce the image contrast (Walther and Humphreys 1997), the ratio of the square root of the ADF intensity in AlGaAs to that of GaAs would be given by $\sqrt{R} \approx 1–9x/32$. This allows us to estimate the Al content of the darkest layers in Figure 3a which are marked in Figure 3b by black upward arrows (where $\sqrt{R} = 0.914 \pm 0.003$) to be $x \approx 0.31$. If the intensity measured in the experiment were reduced by the finite collection angle and inelastic scattering to an exponent Z^n, $n < 2$, this value would increase slightly to $x = 0.34$ (for $n = 1.8$) or 0.38 (for $n = 1.6$), giving an estimate of $x = 0.34 \pm 0.04$. Also, we can see that the first layers grown thereafter (marked by grey downward arrows) have a slightly reduced intensity compared to all other GaAs layers ($\sqrt{R} = 0.975 \pm 0.004$), which could indicate that some Al has diffused into these supposedly pure GaAs quantum wells (with $x \approx 0.09$).

Figure 4 shows a high-resolution TEM (HREM) lattice image of one period with layer thicknesses estimated manually from image intensity variations, where the lattice fringes faintly visible serve only as a precise built-in calibration of the magnification. Measurements of full widths at half maximum (FWHM) from intensity profiles are hardly more accurate than ± 0.4 nm (despite the two figures after the comma from the output of the software Digital Micrograph), however, the values indicated differ from the nominal values only by about 0.3 ± 0.2 nm (mean and rms spread of differences). Note that the overall contrast is reduced in the right half of the image, due to a thickness gradient running obliquely through its middle.

For better lattice imaging, the aberration corrected JEOL R005 instrument was used at 300 kV. Figure 5a shows a high-resolution electron microscopy (HREM) lattice image recorded at higher nominal magnification along the <100> zone axis with near-planar illumination in slight underfocus. Given the above mentioned tilt necessary for the acquisition of figure 3, the layers will now be imaged 2 ° tilted with respect to the electron beam direction. The AlGaAs can be distinguished from the GaAs by the presence of stronger (020) and (002) fringes, and in the top where the specimen is estimated to be only ~10nm thin, by the absence of any (022) fringes, which are, however, dominating the GaAs. In the lower half the specimen is slightly thicker, close to ~ 15 nm where the {022} fringes disappear in both materials. At this specimen thickness a 2 ° layer tilt with respect to the zone axis will introduce a slight blur of the interfaces, of the order of 0.5 nm or two group III bilayers, as given by the product of specimen thickness and tangent of the inclination angle. For the top region, the corresponding uni-directional blur will only be ~ 0.35 nm and thus be confined to adjacent bilayers, which is negligible. Figure 5b is a Bragg filtered version of 5a

where only the (020) and (002) reflections are admitted before back-transformation (with a Gaussian shaped mask filter to avoid edge artefacts due to the filtering). The layers are well discernible, in particular in the thinner top half, and display short terraces on (002) as well as facets on inclined (022) and ($0\bar{2}2$) planes. A pattern recognition algorithm was then used to map and measure the sum of the amplitudes of (020) and (002) lattice fringes in each image unit cell centred on an atomic column of group-III atoms, as used previously to map the Al distribution in AlGaAs/GaAs layers at 400 kV (Walther and Gerthsen 1993) and which gave atomic sensitivity at optimal thicknesses around 10-15nm (Walther et al. 1995). The result is shown on in Figure 5c. The contrast increases from a minimum of 1.05 in GaAs to 14.37 in AlGaAs (where the mean image intensity on an 8 bit grey scale is 142.3, with a standard deviation of 21.5 counts). If we assume that in this ~ 10 nm thin region the kinematical approximation is still valid, according to which the {002} contrast is proportional to the square of the difference in the atomic numbers of group-III and and group-V sub-lattices, and the lowest value close to zero relates to pure GaAs, then the ~14 times higher contrast in $Al_xGa_{1-x}As$ would correspond to $x = 0.30$ instead of the nominal value of 0.45. This agrees with the above estimate from ADF STEM. Interpolating the local Al content in image unit cells between those in binary GaAs for $x = 0$ and those in the middle of the widest $Al_xGa_{1-x}As$ barrier for $x = 0.3$ as references, would give a fully quantitative compositional map of the region observed. As the image reveals considerable roughness on the atomic scale, this will probably also be true along the electron beam direction and, together with the above 2 º layer tilt, could partly explain the apparent reduction in aluminium content as a projection effect rather than a result from interdiffusion.

Finally, if we use aberration-corrected ADF-STEM we can directly resolve all atomic columns and identify AlGaAs on the basis of the Al-rich group-III atomic columns having the lowest atomic number. We have recorded such images along the same <100> zone axis in the aberration corrected JEOL 3100Z R005 microscope at 300 kV, one of which is shown in Figure 6a. In order to avoid beam damage, we have used a low beam current (~10 pA) and short exposure time (12 µs dwell time per pixel) so the image appears rather noisy. Figure 6b is again a Bragg filtered version of (a), this time admitting all Bragg reflections and just eliminating shot noise, so the layers are easily distinguishable on the basis of both their different scattering power and pattern, as the Al-rich atomic columns are almost invisible. One can discern an average ~ 7 º tilt of the layers with respect to the (002) lattice planes in the image due to the substrate offcut, and in particular the upper interfaces of the AlGaAs (GaAs-on-AlGaAs) appear rough on the atomic scale. We have then processed the raw image as follows: To eliminate the dark line features in (a), which are due to fluctuations of the emission current of the cold field emission gun during the recording, we have divided each individual line of the image by its average intensity value. We have then fitted a mesh to the lattice based on the positions of the brightest (As) columns (with an rms spread of ~ 2 pixels) and determined the intensity of each group-III column in-between by integration of intensity around the 'tunnel sites' over a radius of 3 pixels. This is similar to the procedure of column ratio mapping used by Finnie, Craven and Robb (2009) for AlAs/GaAs imaged along <110> although the treatment of the background intensity is slightly different. The resulting map in Figure 6c has a maximum of 10.5 (corresponding to pure Ga: $Z = 31$) and a minimum of 6.82 (corresponding to mixed Al/Ga columns with $\langle Z \rangle = 31-18x$). If we again consider the intensity of the group-III columns is proportional to Z^n with a power exponent of n

then we can infer a maximum Al content of $x = 0.41$ ($n = 1.6$), 0.37 ($n = 1.8$) or 0.33 ($n = 2$, the ideal case of Rutherford scattering), i.e. $x = 0.37 \pm 0.04$. This is, again, in agreement with the above estimates of $x = 0.30$ from HREM Fourier analysis and of $x = 0.34 \pm 0.04$ from ADF STEM contrast without lattice resolution, similar to what was reported in an earlier comparison of low and high-resolution ADF STEM contrast for InGaAs (Qiu et al. 2011).

As the specimen region used for high-resolution STEM in figure 6 was slightly thicker than the one used for HREM in figure 5, ~ 15-30 nm from intensity estimates, the blur due to the 2 ° misorientation of the layers with respect to the <100> zone axis can amount to 0.5-1.0 nm and is probably responsible for the significant apparent loss of image contrast in the lower right part of figure 6c. For even thicker regions the thinnest layers would have been completely obscured by the offcut.

For the nominal offcut of 10 ° towards {111} this would have produced interfaces on {118} habit planes which could have been imaged edge-on by cutting the original wafer so as to produce a $[\bar{1}10]$ oriented specimen with the offcut direction lying in the specimen plane. However, as we have seen the real offcut was ~ 7 ° towards [010] but only 2 ° towards [100], giving an effective smaller offcut of only 7.3 °. The Miller indices of the real interface habit planes are therefore expected to lie closer to {1 3 25} and would ideally have necessitated an investigation along a $[\bar{3}10]$ zone axis instead.

In addition to the offcut problem, the contrast reduction in the right part of figure 4 and the lower parts of figures 5 and 6 is probably in part due to some surface contamination, as we found evidence of preferential carbon deposition in or near the investigated regions from STEM overview images taken after the high-resolution analyses. This is expected to slightly reduce the apparent lattice fringe contrast in both HREM and STEM modes, however, as this will apply to AlGaAs and GaAs to the same degree the relative lattice contrast changes evaluated above and the corresponding interpretation should not change.

A much more serious problem could potentially be preferential oxidation (Al-rich AlGaAs is known to oxidise more rapidly than GaAs, cf. Alay and Vandervorst, 1992) as this could reduce the crystalline thickness of AlGaAs regions more than that of GaAs and so would reduce its lattice contrast more than that of GaAs, however, we found no evidence for preferential oxidation in our sample.

Conclusion

We have shown by comparison of different TEM imaging methods using calibrated magnifications that

i) the growth rate of the stacks varied slightly (± 1 nm) during growth, where stacks grown in the beginning and towards the end were ~ 2 nm (4 %) thinner than stacks in the centre, which may lead to optical emission broadening and

ii) the average stack periodicity and the AlGaAs barrier layer thicknesses agreed with the nominal values, within error bars of one group-III layer thickness, so that the electron quantum confinement should be as modelled.

Quantitative contrast mapping of HREM and ADF STEM showed that

iii) there was indication of facetted growth, due to the offcut, with the top of the AlGaAs being rougher or more diffuse than the top of the GaAs layers;

iv) the Al content of the AlGaAs barriers was slightly lower than expected (x = 0.3-0.4 instead of 0.45), which may enhance the electron tunnelling probability slightly.

References

Alay, J.L. and Vandervorst, W. (1992) X-ray photoelectron–spectroscopy analysis of ion-beam-induced oxidation of GaAs and AlGaAs. *J. Vac. Sci. & Technol.* **10**:4, 2926-2930.

Barvosa-Carter W, Twigg ME, Yang MJ and Whitman LJ (2001) Microscopic characterization of InAs/$In_{0.28}Ga_{0.72}Sb$/InAs/AlSb laser structure interfaces. *Phys. Rev. B* **63**, 245311.

Cao J-C, Li H, Han Y-J, Tan Z-Y, Lü J-T, Luo H, Laframboise S and Liu H-C (2008) Terahertz quantum cascade laser at 3.39 THz. *Chin. Phys. Lett.* **25**:3, 953-956.

Faist J, Capasso F, Sivco DL, Sirtori C, Hutchinson AL and Cho AY (1994) Quantum cascade laser. *Science* **264**: 5158, 553-556.

Finnie M, Craven AJ and Robb PD (2010) A HAADF investigation of AlAs/GaAs interface using SuperSTEM. Proc. EMAG 2009, Sheffield. *J. Phys. Conf. Ser.* **241**, 012049.

Green RP, Wilson LR, Zibik EA, Revin DG, Cockburn JW, Pfügl C, Schrenk W, Strasser G, Krysa AB, Roberts JS, Tey CM and Cullis AG (2004) High-performance distributed feedback quantum cascade lasers grown by metalorganic vapor phase epitaxy. *Appl. Phys. Lett.* **85**, 5529-5531.

Hue F, Johnson CL, Lartigue-Korinek S, Wang G , Buseck PR and Hytch MJ (2005) Calibration of projector lens distortions. *J. Electron Microsc.* **54**:3, 181-190.

Inoue Y, Nagasawa H, Sone N, Ishino K, Ishida A, Fujiyasu H, Kim JJ, Makino H, Yao T, Sakakibara S and Kuwabara M (2004) Fabrication and characterization of short period AlN/GaN quantum cascade laser structures. *J. Cryst. Growth* **265**:1-2, 65-70**.**

Kandaswamy PK, Guillot F, Bellet-Amalric E, Monroy E, Nevou L, Tchernycheva M, Michon A, Julien FH, Baumann E, Giorgetta FR, Hofstetter D, Remmele T, Albrecht M, Birner S and Dang LS (2008) GaN/AlN short-period superlattices for intersubband optoelectronics: a systematic study of their epitaxial growth, design, and performance. *J. Appl. Phys.* **104**, 093501.

Krysa AB, Revin DG, Commin JP, Atkins CN, Kennedy K, Qiu Y, Walther T and Cockburn JW (2011) Room temperature GaAs/AlGaAs quantum cascade lasers grown by metal-organic vapor phase epitaxy. *IEEE Photon. Technol. Lett.* **23**:12, 774-776.

Liu F-Q, Yong Y-Z, Zhang Q-S, Ding D, Xu B, Wang Z-G, Jiang D-S and Sun B-Q (2000) high-performance strain compensated InGaAs/InAlAs quantum cascade lasers. *Semicond. Sci. Technol.* **15**, L44-L46.

Manz C, Yang Q, Köhler K, Maier M, Kirste L, Wagner J, Send W and Gerthsen D (2005) High-quality GaInAs/AlAsSb quantum cascade lasers grown by molecular beam epitaxy in continuous growth mode. *J. Cryst. Growth* **280**, 75-80.

Matmon G, Paul DJ, Lever L, Califano M, Ikonic Z, Kelsall RW, Zhang J, Chrastina D, Isella G, von Känel H, Müller E and Neels A (2010) Si/SiGe quantum cascade superlattice designs for terahertz emission. *J. Appl. Phys.* **107**, 053109.

Pennycook SJ and Jesson DE (1991) High-resolution Z-contrast imaging of crystals. *Ultramicroscopy* **37**:1-4, 14-38.

Qiu Y, Lari L, Ross IM and Walther T (2011) Comparison of the contrast in conventional and lattice resolved ADF STEM images of InGaAs/GaAs structures using different camera lengths. Proc. 17th Conf. Microsc. of Semiconducting Materials, Cambridge. *J. Phys. Conf. Ser.* **326**, 012041.

Revin DG, Kennedy, K, Commin JP, Qiu Y, Walther T , Cockburn JW and Krysa AB (2011) High temperature $\lambda \sim 4$ μm $In_{0.7}Ga_{0.3}As/In_{0.34}Al_{0.66}As$ quantum cascade lasers grown by MOVPE. *Electron. Lett*. **47**:9, 559-561.

Terashima W and Hirayama H (2009) design and fabrication of terahertz quantum cascade laser structure based on III-nitride semiconductors. *Phys. Stat. Sol. C* **6**:S2, S615-S618.

Tonouchi M (2007) Cutting-edge terahertz technology. *Nature Photonics* **1**:2, 97-105.

Walther T and Gerthsen D (1993) Quantitative characterization of AlAs / GaAs interfaces by high-resolution transmission electron microscopy along the [100] and [110] projection, *Appl. Phys. A* **57** (1993) 393-400.

Walther T, Humphreys CJ, Grimshaw MP and Churchill AC (1995) Detection of random alloy fluctuations in high-resolution transmission electron-micrographs of AlGaAs. *Philos. Mag. A* **72**:4, 1015-1030.

Walther T and Humprehys CJ (1997) Quantification of the composition of silicon germanium// silicon structures by high-angle annular dark-field imaging. Proc. EMAG'97, Cambridge. *Inst. Phys. Conf. Ser.* **153**, 303-306.

Walther T (2006) A new experimental procedure to quantify annular dark field images in scanning transmission electron microscopy. *J. Microsc.* **221**:2, 137-144.

Xu DP, D'Souza M, Shin JC, Mawst LJ and Botez D (2008) InGaAs/GaAsP/AlGaAs, deep-well, quantum-cascade light-emitting structures grown by metalorganic chemical vapour deposition. *J. Cryst. Growth* **310**:7-9, 2370-2376.

Table

position	BF/DF-TEM	ADF-STEM	HREM
top	45.0 ± 0.6 (21)	44.7 ± 0.4 (13)	45.1 ± 1.1 (8)
centre	-	47.2 ± 0.7 (36)	-
bottom	-	45.0 ± 0.6 (5)	45.9 ± 1.0 (2)

Table 1: periods measured throughout the stacks. Values are mean values and standard deviations, both given in nm, averaged over a certain number of measurements (given in brackets). Weighted average value overall: 45.8 ± 1.1 nm

Figures

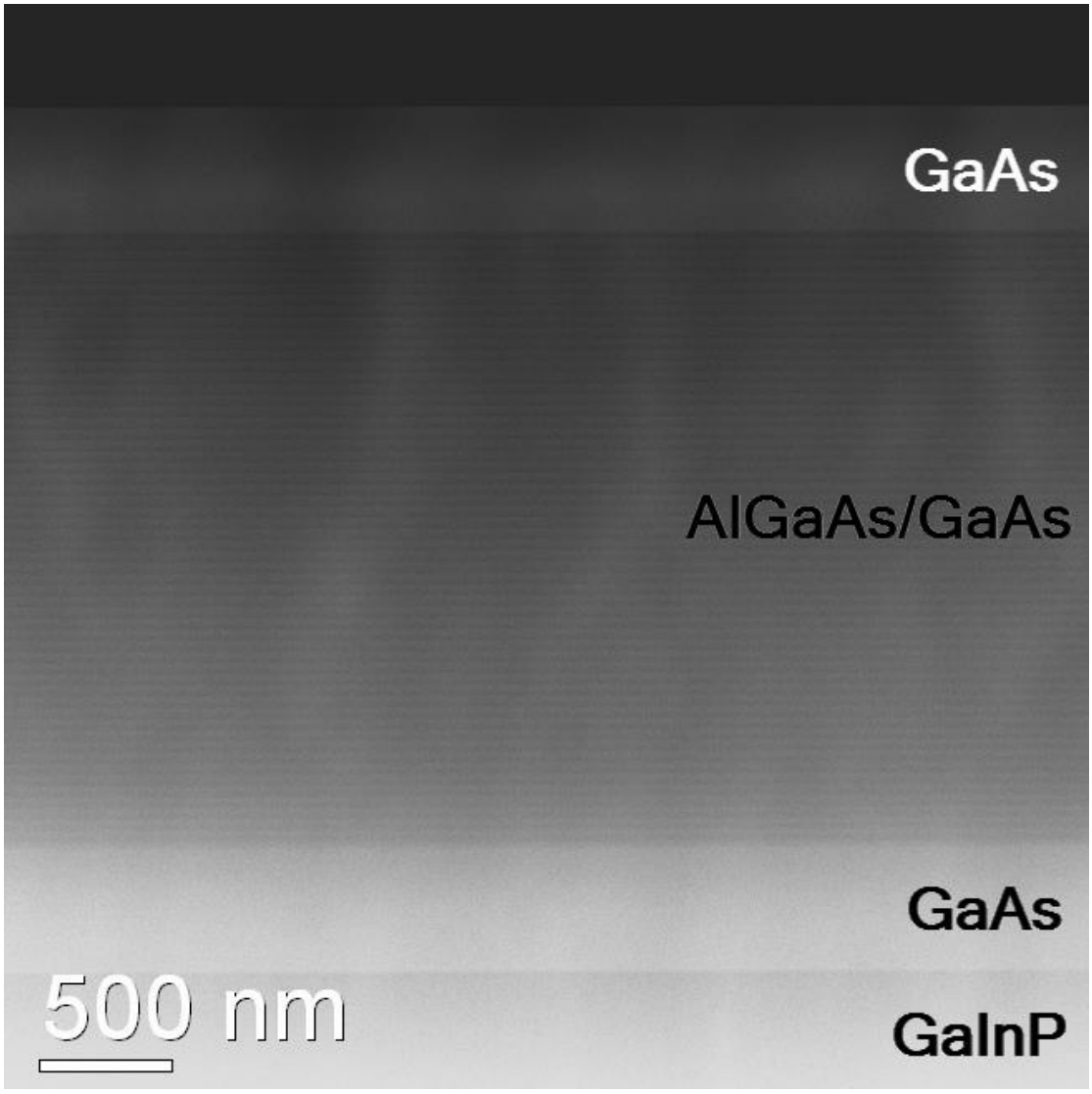

Figure 1: ADF STEM overview (acceleration voltage: $U = 197$kV, nominal magnification: M=15kX, convergence semi-angle: $\alpha = 10$ mrad, collection angle: $\beta = 35\text{-}170$ mrad). Growth direction points upwards. The 55 periods can just be seen. No dislocations are visible over an area of ~ 10 μm^2.

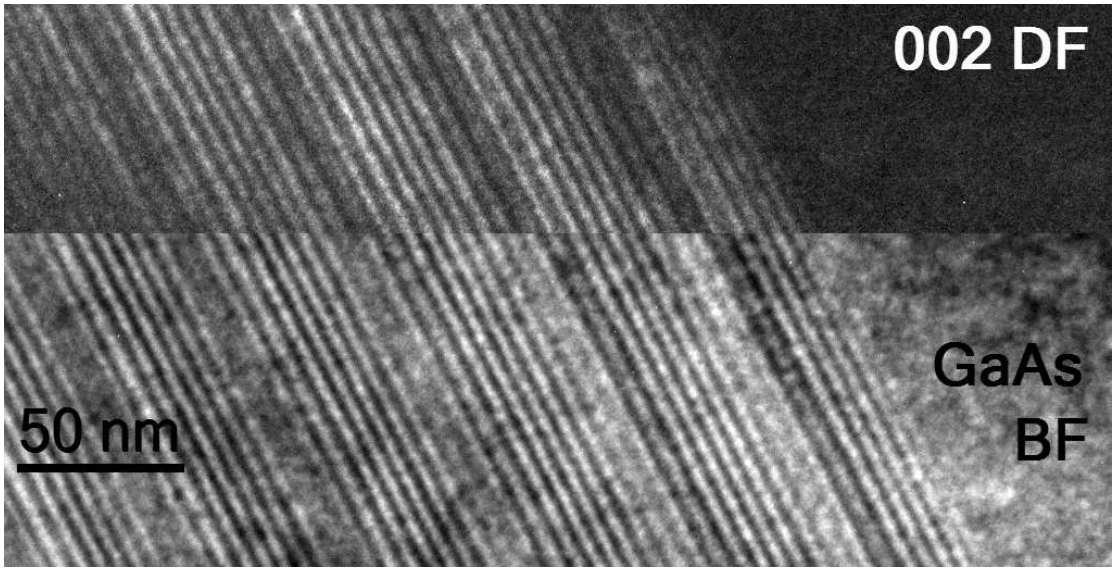

Figure 2: Pair of BF (bottom) and 002 DF (top) TEM images showing the top four periods of the stack, with AlGaAs layers appearing bright (U = 300 kV, M = 60 kX)

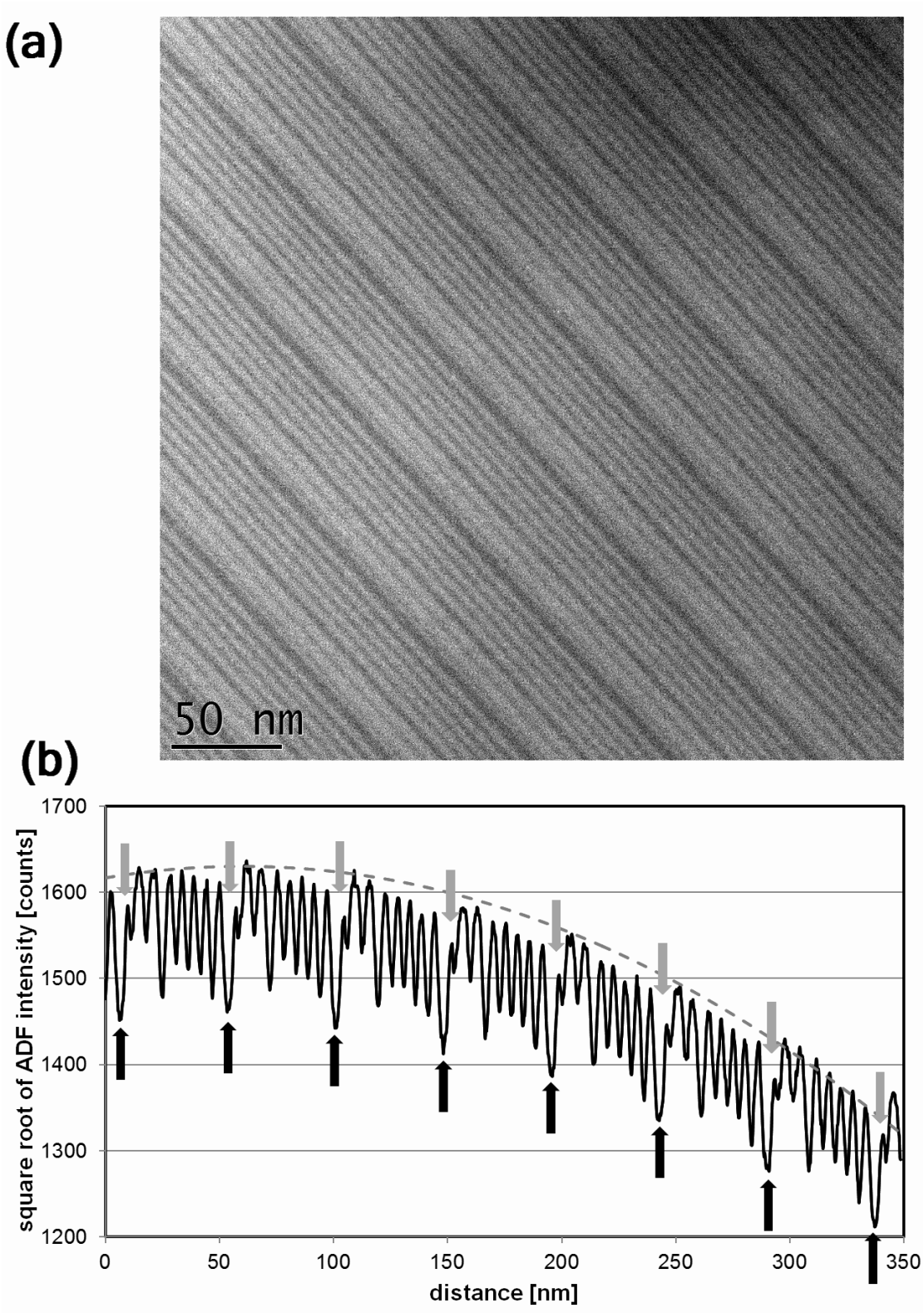

Figure 3: ADF STEM (U = 197 kV, M = 500 kX, α = 10 mrad, β = 55-170 mrad, sampling 0.328 nm/pixel), with line profile of square root of intensity along growth direction.

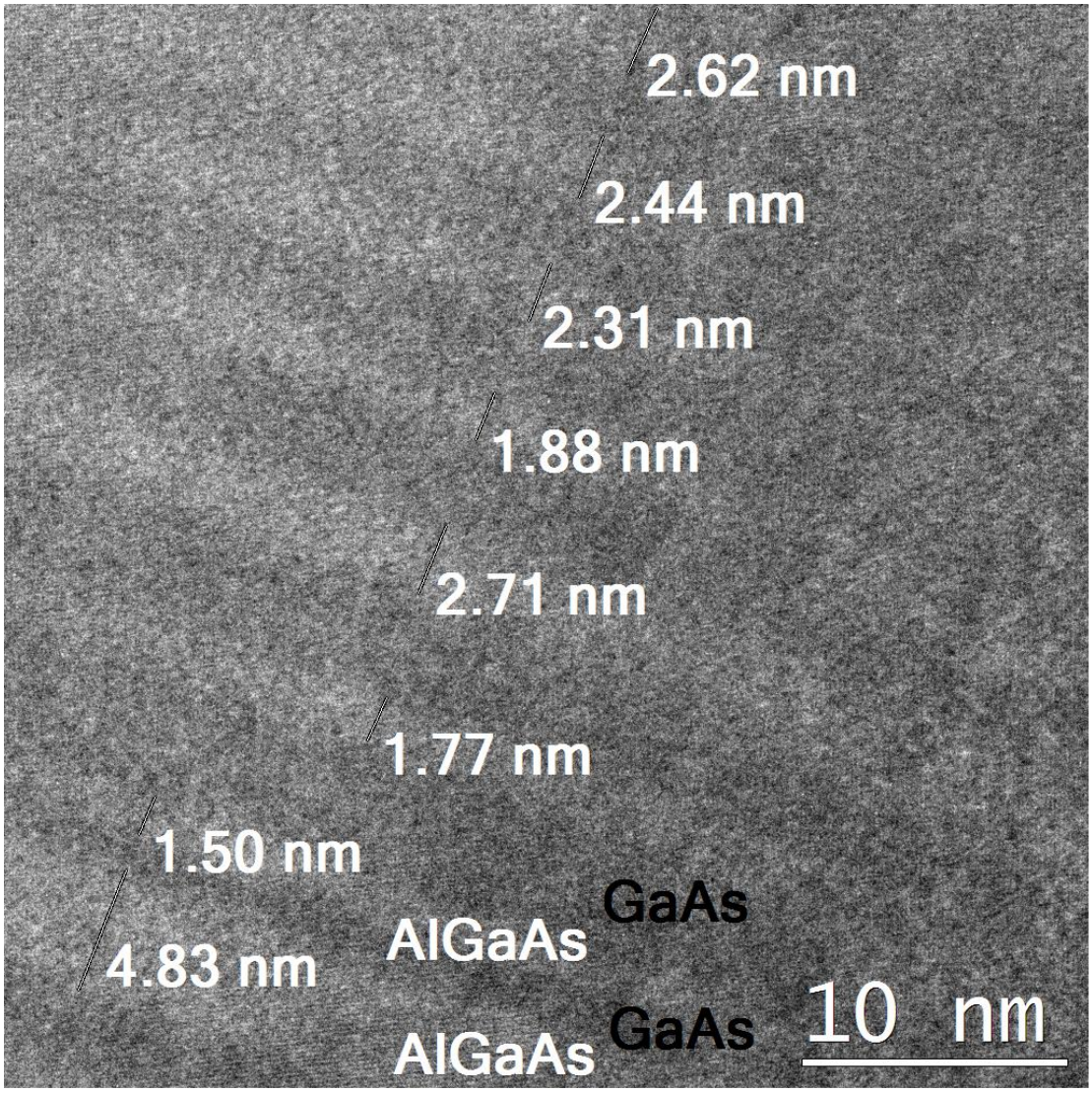

Figure 4: HREM with approximate thicknesses of AlGaAs layers indicated (U = 197 kV, M = 500 kX, β = 20 mrad).

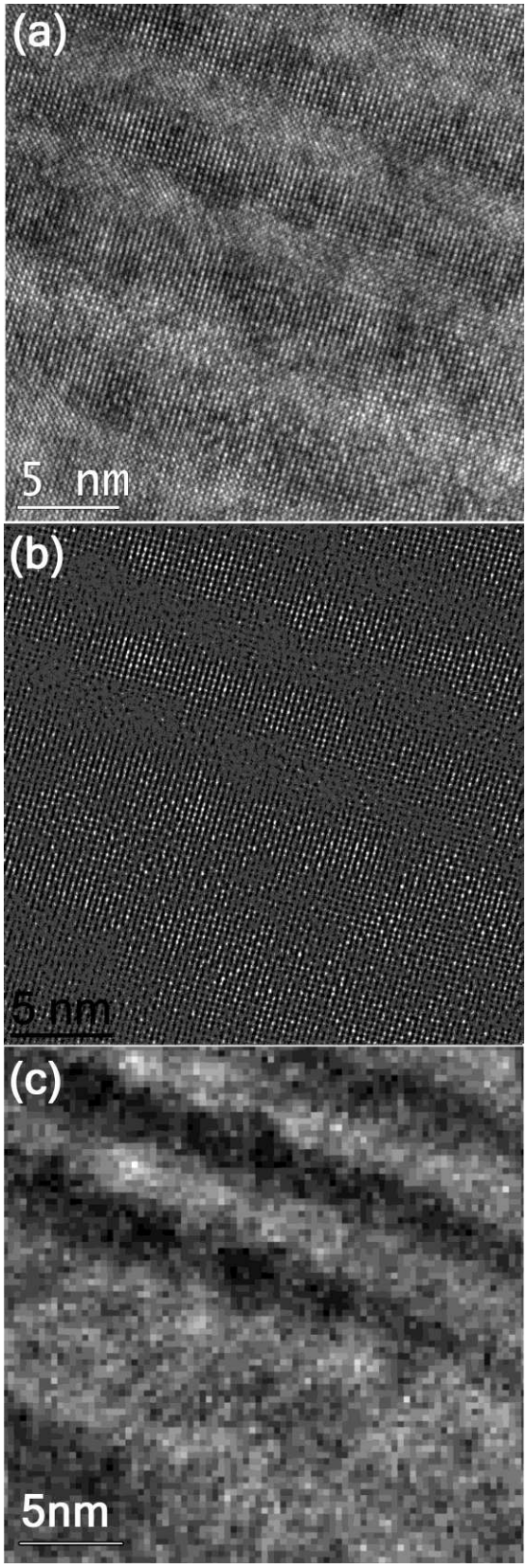

Figure 5: HREM near top of stack showing lattice fringes (U = 300 kV, M = 800 kX). (a) raw image, (b) Bragg filtered image and (c) processed map of the local 002 Fourier amplitudes, with the Al-rich atomic columns bright due to structure factor contrast. The misorientation of the (002) lattice fringes compared to the growth direction is due to the offcut of the substrate.

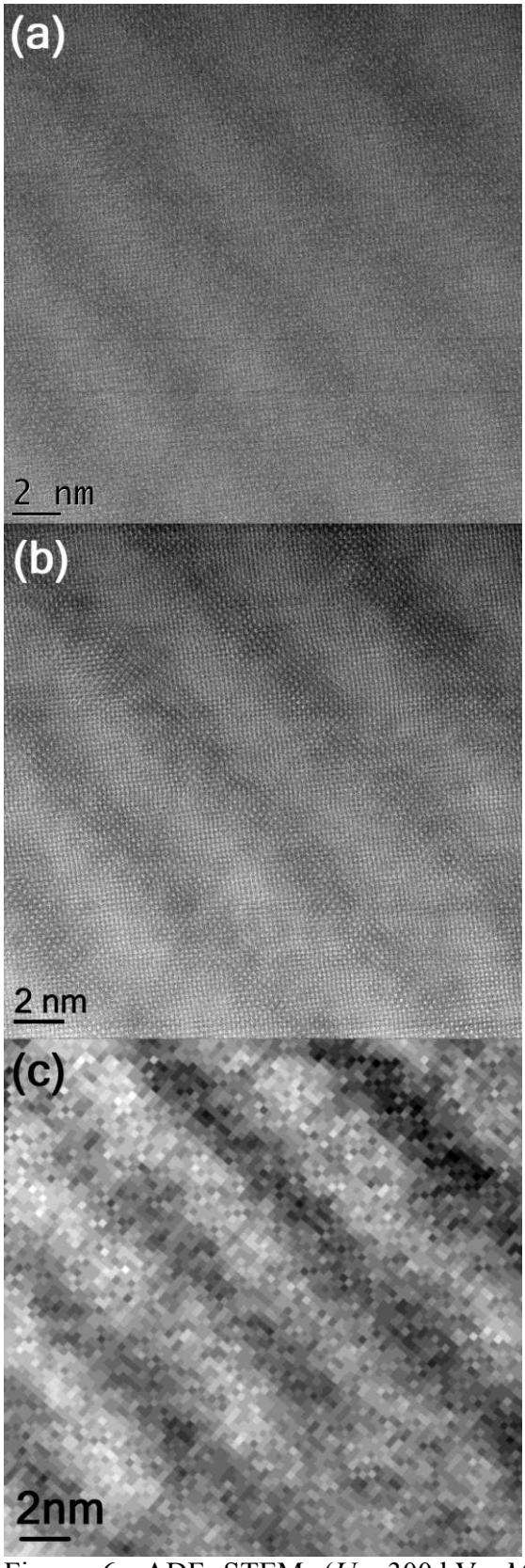

Figure 6: ADF STEM (U = 300 kV, M = 8MX, α = 21 mrad, β = 55-170 mrad), showing {022} and {002} lattice fringes. The patterns are similar to those of Figure 5, but here the Al-rich atomic columns appear dark. (a) raw image, (b) Bragg filtered image, (c) local intensity map of all group-III atomic columns after removal of the

line artefacts in (a) due to emission fluctuations of the cold FEG (see text for more details).